Journal of Cultural Heritage 76 (2025) 100–110

Contents lists available at ScienceDirect

Journal of Cultural Heritage

journal homepage: www.elsevier.com/locate/culher

Original article

Embedding of X-ray computed tomography data of cultural heritage objects in interactive web applications – old technical instruments brought back to novel virtual life

Pia Götz[a,b], David Melamed[c], Hendrik Bohling[c], Christine Brovkina[f], Istabraq Hussain[f], Nils Reims[e], Luca Junge[d], Dennis Hoffmann[d], Karolin Wiskandt[d], Ruth Schilling[d], Martin Hering-Bertram[c], Lucio Colombi Ciacchi[a,b,*]

[a] Hybrid Materials Interfaces Group, Faculty of Production Engineering, University of Bremen, Bibliothekstraße 1, Bremen, 28359, Germany
[b] MAPEX Center for Materials and Processes, University of Bremen, Bibliothekstraße 1, Bremen, 28359, Germany
[c] University of Applied Sciences Bremen, Neustadtswall 30, Bremen, 28199, Germany
[d] German Maritime Museum Leibniz Institute for Maritime History, Hans-Scharoun-Platz 1, Bremerhaven, 27568, Germany
[e] Fraunhofer Institute for Integrated Circuits IIC, Development Center X-ray Technology EZRT, Flugplatzstraße 75, Fürth, 90768, Germany
[f] University of the Arts Bremen, Am Speicher XI 8, Bremen, 28217, Germany

ARTICLE INFO

Article history:
Received 16 March 2025
Accepted 9 September 2025

Keywords:
Maritime history
Technical instruments
Computer tomography
Photogrammetry
Digital preservation
Interactive exhibition

ABSTRACT

X-ray computed tomography (CT) has become a common method for conservators, historians and archaeologists to examine the interior of museum objects in a non-destructive way. This paper demonstrates an additional application of CT data sets. We namely show how the data can be processed and converted to interactive, computer-animated models embedded in web applications to bring back the historical objects to novel virtual life. This opens up a new way for museum visitors to interact with the virtual objects in both on-site and online exhibitions. The use of freely accessible software at all stages ensures that the involved costs remain accessible to public institutions. The approach is demonstrated using three technical instruments of historical significance spanning three centuries of maritime navigation: a pocket sundial, a maritime chronometer, and a pocket barometer manufactured in the 18th, 19th and early 20th centuries. Each object presents its own attributes and characteristics that require different approaches and solutions along the data process chains. The outcomes of these chains are interactive applications demonstrating the functionalities of the old instruments. This contributes to a better understanding of their modes of operation, and can focus the attention of the visitors to individual technical details, material composition and appearance, or other attributes of historical significance. The accessibility and appeal of the virtual objects results in a more immersive interaction experience facilitating a better transfer of knowledge to the visitors.

© 2025 The Authors. Published by Elsevier Masson SAS. This is an open access article under the CC BY license (http://creativecommons.org/licenses/by/4.0/)

1. Introduction

The modern history of maritime navigation is intimately connected with the development of technical instruments used by sailors to estimate the time, the position and the orientation on their ships with increasing accuracy. Before the very recent deployment of satellite-based positioning and signals from automatic identification systems, ingeniously crafted analogue instruments such as chronometers, sundials, and barometers were used. The mechanical precision of their inner mechanisms and the rich variety of materials of which they are composed are not only of large historical and cultural heritage value, but also exert upon interested observers an immediate aesthetic fascination. Old technical instruments are therefore often at the core of museum exhibitions related to maritime history, and curators are exploring new ways of making them and their working principles accessible to a wide public audience, avoiding the risk of irreparable damages.

The advent of digital technologies has enabled the global public to access and interact with high-resolution images and three-dimensional representations of museum collections through computer screens and virtual reality environments [1]. Digitisation of

* Corresponding author.
E-mail address: colombi@hmi.uni-bremen.de (L. Colombi Ciacchi).

https://doi.org/10.1016/j.culher.2025.09.007
1296-2074/© 2025 The Authors. Published by Elsevier Masson SAS. This is an open access article under the CC BY license (http://creativecommons.org/licenses/by/4.0/)

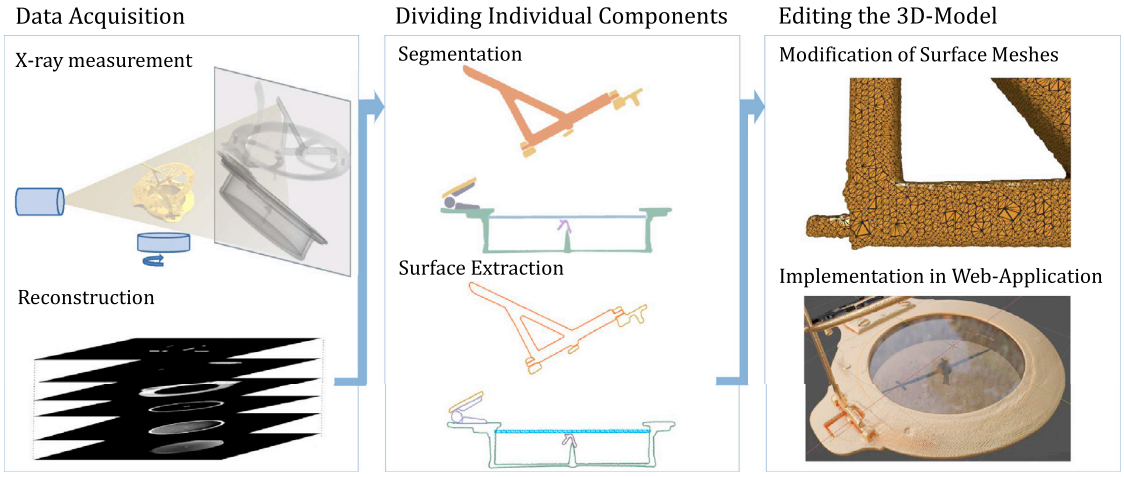

Fig. 1. Schematic flow diagram of the production chain — 1st step (left): data acquisition including X-ray computed tomograhy measurements and reconstruction of the data; 2nd step (centre): dividing individual components involves segmentation of the single parts of the object and its surface extraction; 3rd step (right): editing the 3D model including modification of the surface models and implementation in web-application.

museum exhibits, in particular technical instruments, allows both visitors and scientists to learn about their past and is pivotal in making decisions for their future in terms of conservation [2]. Nowadays, digitisation and non-destructive analyses are ubiquitous tools for the purpose of archiving museum collections and improving their accessibility to visitors both on-site and online [1,3–6].

For several decades, surface models of cultural heritage objects based on photogrammetric measurements have been employed in museums to conserve and present valuable objects in digital form [7,8]. The 3D photogrammetric reconstructions contain information about the topography and colour of the exposed object surfaces. The digital objects can be rendered as sets of surface meshes on 3D viewer platforms such as Sketchfab [9]. Sketchfab provides a web-based viewer giving users the ability to remotely display objects as 3D models and examine them through interactive actions such as dragging and rotating. In order to demonstrate the mechanical function of historical measurement devices, however, we also need further information about their interior, not only of their exposed surfaces.

X-ray computed tomography (CT) is a non-destructive analysis method that has been used in applications as varied as medicine [10,11], materials testing [12,13], climatology [14,15], geology [16], and archaeology [2,17–20]. Since CT generates digital images of both the overall structure and the interior of objects, it is increasingly employed in the cultural heritage sector, besides traditional photogrammetry [21–23]. CT data sets can either be represented as 2D projections from a fixed perspective or, after appropriate rendering, as full 3D models [24]. Typical is the rendering of selected object parts as surface meshes, in the spirit of photogrammetry, although without the information about the true object colour [25]. For instance, the transformation of surface data in PDF format has been proposed to share complex 3D data sets effectively and intuitively between scientists from different fields [26]. However, when it comes to visualising parts of the objects moving in relation to each other, for example to show how an old measuring instrument works, more interactive workflows are necessary.

In the present work, we describe the process of preparing computer-animated, interactive views of multiple devices that allow a broad public to examine them and understand both their history and their working principles. The most important steps in this process are depicted in Fig. 1. First, after the acquisition of the raw 3D data by X-ray measurements and reconstruction, the single components of the instruments need to be digitally separated in the so-called segmentation process. Then, the surface models are extracted, digitally repaired wherever necessary, and equipped with physically meaningful kinematic properties. Afterwards, the parts are digitally assembled and rendered in a realistic representation. Finally, the model is implemented in web applications giving the end users such as museum's visitors an immersive experience of interaction with the old instruments in their new digital life. This leads to a better understanding of how these old instruments appeared and worked, even when the original objects are not physically accessible or defective.

In the following, we demonstrate this workflow with three historical technical instruments belonging to the collection of the German Maritime Museum, Leibniz Institute for Maritime History in Bremerhaven, Germany: a pocket sundial, a maritime chronometer and a pocket barometer, which will be described in more detail in the next sections (Fig. 2). The first two were used to measure time and time differences that were crucial for ship navigation before the widespread use of modern satellite-based systems. The latter was used to measure pressure changes to assess weather conditions and to determine the altitude in aeroplane and mountain expeditions. The entire workflow, from the initial segmentation up to the web implementation, is carried out by means of free software solutions (listed in the Supplementary Information), leading to interactive applications accessible to common mobile and desktop browsers.

2. Research aim

The aim of this work is to develop and apply a comprehensive workflow for the creation of interactive and animated three-dimensional digital representations of technical instruments used in ancient maritime navigation. The advantages and limitations of measurement techniques based on a combination of computed tomography and structured-light scanning are explained and practically addressed. It is shown how the acquired data require elaboration and augmentation with the help of freely available software in order to improve the quality of the final outcome and produce data sets of manageable size. Further, the issues associated with the modelling and implementation of the digital representations in publicly accessible online applications are addressed in three different scenarios. As a result, the mechanical functions and material compositions of a maritime chronometer, a pocket sundial and a pocket barometer are presented to a wide online audience. In this

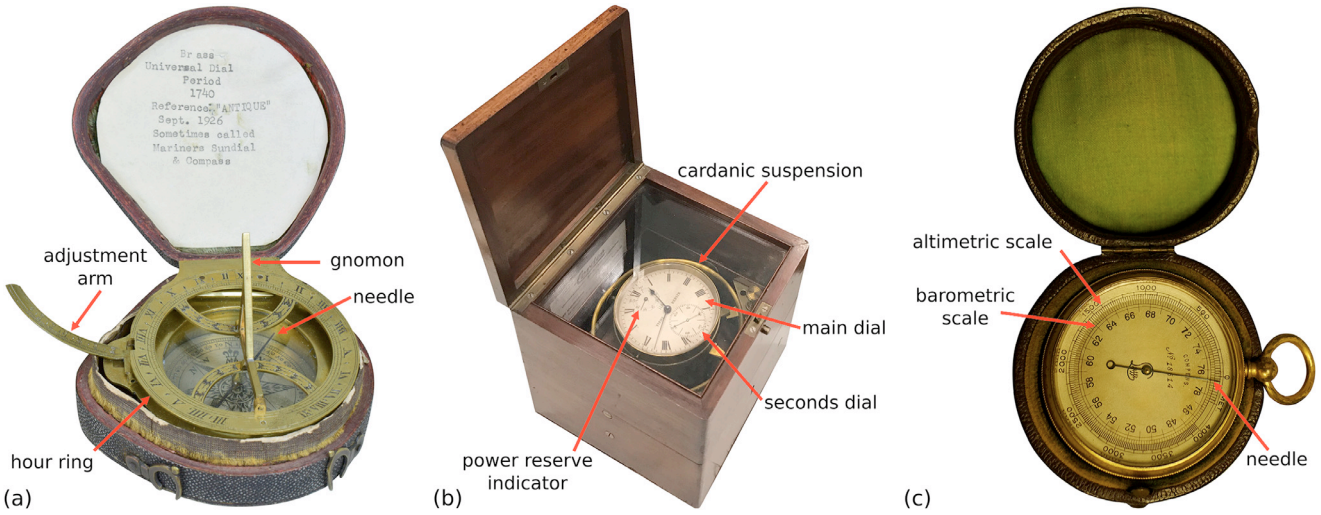

Fig. 2. Photographs of the three historical instruments that have been digitised: (a) pocket sundial from 1740, made of brass in a shagreen case; (b) Tiede's maritime chronometer from 1835–1840; (c) Lufft pocket barometer from the early 20th century.

way, a realistic and accurate perception of the devices is facilitated, enhancing the appreciation of their cultural heritage value.

3. Material and methods

3.1. Museum objects

Our three objects originate from the collection of the German Maritime Museum, Leibniz Institute for Maritime History, Bremerhaven, Germany.

3.1.1. Pocket sundial

The pocket sundial (Fig. 2a) was crafted from brass and housed in a shagreen case. The labelling on a paper insert in the interior of the case's lid indicates that the item may have been manufactured as early as 1740, with a probable location in England. The arm for the adjustment of the latitude, the hour ring and the gnomon can be folded into the case for the purpose of transportation. The hour ring, marked at 5-min intervals, shows engraved and black–coloured Roman numerals. Underneath the hour ring, a compass consisting of a blued steel needle and a compass rose (presumably also made of brass) is protected by a glass crystal.

3.1.2. Maritime chronometer

The chronometer (Fig. 2b) was crafted between 1835 and 1840 in Berlin by the manufacturer Christian Friedrich Tiede. The housing is constructed from brass and is cardanically balanced within a wooden case, thereby enabling precise time determinations to be made on a rolling ship. The wooden case is equipped with two hinged and lockable lids: opening the top lid enables the instrument to be read, while opening the bottom lid allows the power spring to be wound. The chronometer is equipped with a main dial for the hour and the minute hands and two additional dials within it: the upper one for the power reserve indicator of the spring tension, and the lower one for the seconds hand. The dials are protected by a glass crystal.

3.1.3. Pocket barometer

The pocket barometer (Fig. 2c) was manufactured in the early 20th century by Gotthilf Lufft in Stuttgart, Germany, and carries the serial number 18514. The device is calibrated in centimetres of mercury (cmHg) with a range from 46 to 78 cmHg, divided into 2 mmHg increments. The outer altimetric scale encompasses a range from 0 to 4000 metres, divided into 20-metre intervals. The corresponding values are indicated by a blued steel pointer (or needle). The brass housing is protected by a glass crystal and encased in a leather case, which is in turn lined with velvet fabric.

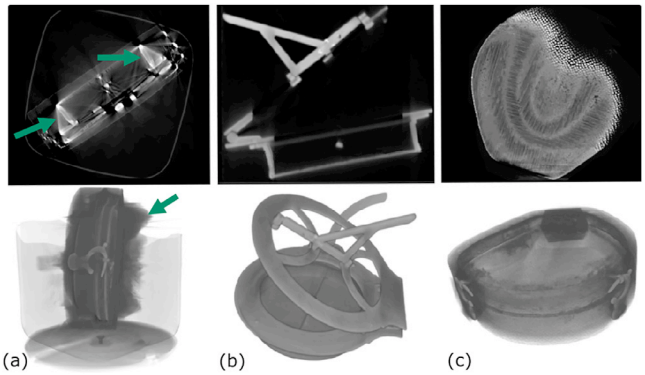

Fig. 3. Different intensities of the X-ray computed tomography measurement of the pocket sundial as a 2D grey value slide (top row) and a 3D rendering (bottom row): (a) measurement result of the folded sundial with rather low intensities (ProCon CT-Alpha), leading to streaking artefacts visible inside and outside the sundial (green arrows); (b) measurement of the unfolded sundial with higher X-ray energies (HE-CT); (c) case made of lighter material measured separately with lower energies (ProCon CT-Alpha). (For interpretation of the references to colour in this figure legend, the reader is referred to the web version of this article.)

3.2. Data acquisition and processing

3.2.1. X-Ray Computed tomography measurements

The three objects were measured with the high-energy CT (HE-CT) of the Fraunhofer Institute for Integrated Circuits, with a peak voltage of 7.8 MeV, an exposure time of one second per frame and a resulting voxel size of 181 μm. In order to compare the influence of high versus low intensity (vide infra, Section 4.1 and Fig. 3), the pocket sundial was additionally measured with a ProCon CT-Alpha at the MAPEX Center for Materials and Processes at the University of Bremen. The measurement parameters included a voltage of 115 kV and an exposure time of 0.5 s with six frames per projection, resulting in a voxel size of 60.8 μm. The case of the pocket sundial was separately measured with the ProCon CT-Alpha with a voltage of 130 kV and an exposure time of 0.35 s with six frames per projection, resulting in a voxel size of 52.6 μm. Both devices

Table 1
X-ray CT measurement parameters used for scanning the pocket sundial, the case of the pocket sundial, the pocket barometer, and the maritime chronometer.

Object	Measurement device	Peak voltage [kV]	Power [W]	Pulse rate [Hz]	SOD [mm]	SDD [mm]	Bin.	Exp. [s]	Proj.	FPP	voxel size [µm]
Pocket sundial	CT-Alpha	115	34.5	–	370	754	2	0.50	2000	6	61
Pocket sundial	HE-CT	7800	–	400	3922	4332	1	1.00	1200	1	181
Case p. sundial	CT-Alpha	130	45.5	–	320	754	2	0.35	2560	6	53
Barometer	HE-CT	7800	–	400	3922	4332	1	1.00	1200	1	181
Chronometer	HE-CT	7800	–	400	3922	4332	1	1.00	1600	1	181

SOD = source-to-object distance, SDD = source-to-detector distance, Bin. = binning, Exp. = exposure time per frame, Proj. = number of projection images, and FPP = frames per projection.

operated with a flat panel as the detector. The parameter settings are presented in Table 1.

3.2.2. Reconstruction

The X-ray transmission data sets of the CT-Alpha measurements of the pocket sundial and its case were reconstructed into 16-bit format using X-AID [27]. The data sets of the Fraunhofer HE-CT measurements of the barometer, the sundial and the chronometer were reconstructed with the Firefly Software developed at the Fraunhofer EZRT. After reconstruction, the retained three-dimensional volume of absorbed X-rays encoded in grey values was exported in the lossless Tagged Image File Format (TIFF) as a stack of images.

3.2.3. Segmentation and surface extraction

The stack of TIFF images produced by the reconstruction was segmented into the relevant regions of interest (ROI) with the Dragonfly software version 2020.2, with free licensing for non-commercial users [28]. The same software was used for the extraction of triangulated surface meshes corresponding to each ROI, using variable amounts of triangles. Up-sampling of the reconstructed data and mesh smoothing algorithms were applied before and after triangulation, respectively, for visualisation purposes, as described later in the Results Section. For further manipulation of the surface meshes, they were exported in the OBJ data format and loaded into the 3D graphics software Blender version 3.0.1 [29].

3.2.4. Manipulation of the surface models

Manipulation of the surface models with Blender was carried out both to save storage size by replacing some meshed parts with simple geometric forms and to repair faulty holes in the surface meshes resulting from poor segmentation. Small and fine structures of the objects, whose features were below the resolution limit, were replaced completely by digital ones newly built with Blender, for instance using its extrude function in the 'Edit' mode.

3.2.5. Assignment of a materiality to the surfaces

A realistic appearance of the objects was achieved by assigning specific digital materialities to each meshed model part with the Properties editor of Blender. In addition, settings such as colour, transparency and reflectivity were adjusted to achieve the desired texture and come as close to a natural-appearing material as possible. The final models were then exported as Graphics Library Transmission Format (GLTF) files with Draco compression to reduce the file size for the web applications.

3.2.6. Structured-light 3D scanner

The structured-light 3D scan of the maritime chronometer was created with a Hexagon Smartscan and the OptoCat 21 software at the German Maritime Museum to enhance the surface model of the chronometer with its original photorealistic appearance, especially the details of the wooden case's grain. The sensor was calibrated using the 'S-350' measuring field. The surface images were mapped onto a 2D set of texture coordinates *U* and *V* (*UV* mapping) used to represent each polygon.

3.2.7. Animating 3D models

Presets of automated movements were defined in advance by means of 'keyframes', setting the initial, the final and any important intermediate positions of the movable elements. Such presets were then exported as GLB files that served as input for the three.js web application and formed the basis for the interactive animations therein.

3.3. Implementation in web application

The interactive applications were created with three.js, which is an open-source, cross-platform JavaScript library that uses web standards such as the Web Graphics Library (WebGL) to create 3D scenes [30]. The three.js project was created locally with the aid of NodeJS, which functions as a back-end file host during the development process, thereby producing a build that can subsequently be deployed to a web server. The user interfaces of the web pages were created with HTML and CSS, with further interactions being programmed with pure JavaScript. The three.js library is then responsible for rendering content to the screen and reacting to further interaction with the models.

3.3.1. Model import and application control

The GLTF file format was utilised to integrate the 3D models into the web application. Firstly, the model was decompressed using the Draco add-on of the three.js application. Secondly, the model was loaded via an asynchronous function using the GLTFLoader class. This approach ensures smooth integration without blocking other application processes, ensuring that the web application continues to run while the model loads, thereby enhancing performance and user experience. The user interaction with the three-dimensional models was enabled by an add-on for three.js: the functions of 'OrbitControls' enable rotation, zooming, and panning. The functions were compatible with both mouse and touch inputs, ensuring accessibility across diverse devices.

4. Results

In this section, we follow the workflow depicted in Fig. 1 and describe the key aspects of the surface extraction, remodelling, resolution adaptation, texture mapping, animation, and implementation in web applications of the three historical instruments shown in Fig. 2.

4.1. X-ray measurements

The fundamental basis of the workflow is the utilisation of X-ray CT measurements. Since the objects are composed of materials spanning a wide range of densities corresponding to their different elements (metal, glass, leather, etc.), a corresponding range of X-ray energies and CT settings was required (Table 1). Metallic parts made of elements with high atomic numbers necessitate high energies of the penetrating X-rays to avoid streaking artefacts due to beam-hardening effects. Beam hardening is caused by the

polychromatic (multi-energy) nature of X-ray beams, where lower-energy photons are preferentially absorbed as the beam passes through matter. This leads to a non-linear attenuation and image distortions such as cupping and streak artefacts, especially near high-density structures. These artefacts are visible, for instance, after imaging the pocket sundial with the ProCon CT-Alpha (Fig. 3a). High-signal artefactual streaks appear in the 2D X-ray images in correspondence of metal edges, surrounded by signal-void areas resembling air gaps. This results in non-physical fuzzy and blurred structures in the 3D view (green arrows, Fig. 3a, top). In contrast, the same object imaged with the linear accelerator LINAC of the Fraunhofer Institute for Integrated Circuits, that operates at up to 9 MeV, leads to sharp and nearly artefact-free images and faithful reconstructions (Fig. 3b).

The appropriate energies and instruments depend, in general, on the composition and orientation of the object in the X-ray beam. In particular, dense and compact objects like our pocket sundial should be unfolded, if possible, as was done in the measurement shown in Fig. 3b. On the other hand, low-density objects such as the shagreen case of the sundial are better imaged with lower intensities and at higher resolution, enabling a reliable representation of their fine structure (Fig. 3c).

4.2. Reconstruction

Once the X-ray measurement data have been acquired, the single attenuation images, which were taken at varying angles, must be reconstructed into a three-dimensional model. In order to achieve this objective, a number of different reconstruction software packages are currently available on the market, incorporating data-reading routines for common CT devices. The most basic products merely reconstruct the angle-resolved transmission images into a three-dimensional data set of grey-values assigned to discrete volume elements (so-called voxels) in a cartesian coordinate set. Typically, the data set is stored as two-dimensional plane images (in TIFF format) stacked along one cartesian direction. However, numerous products also offer intelligent algorithms to reduce measurement artefacts (e.g., beam hardening, as illustrated in Fig. 3a, scattering, scan instabilities, geometrical errors, bad pixels/rings) and thus assist in enhancing the overall image quality. The data sets utilised in this study were not subjected to any filtering procedures, as the measurement settings yielded images of sufficient quality.

4.3. Segmentation

In order to isolate specific elements of the imaged objects, the voxels resulting from the reconstruction procedure can be assigned to groups pertaining to those elements. This process is referred to as ‘segmentation’, and the voxel groups defining the spatially isolated elements are called regions of interest (ROI) in the terminology used by the Dragonfly software (v2020.2). The most straightforward approach is to group together voxels with grey values within predefined thresholds, corresponding, e.g., to a certain material density. In many cases, however, it is necessary to distinguish between ROI made of the same material or, in general, exhibiting overlapping ranges of grey values. For example, the adjustment arm, the gnomon and the hour ring of our pocket sundial are all made of brass, but are best represented by different ROI (Fig. 4, left panel). In these cases, it is necessary to undertake manual segmentation procedures, sometimes down to a voxel-by-voxel basis using the Dragonfly software. Presently, novel approaches based on machine-learning algorithms are being developed to facilitate the automatic segmentation of complex objects from CT data sets characterised by analogous grey values [31,32]. These approaches, however, were not employed in the present study.

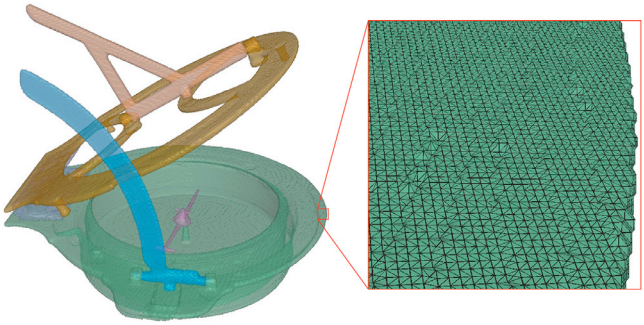

Fig. 4. 3D rendering of segmented parts of the historical pocket sundial and its resulting mesh (left), including a zoom-in (right). Left: bottom housing with its pin (green) balancing the compass needle (mauve), the upper folding ring (yellow), the hinge (purple) connecting the bottom housing with the upper folding ring, the gnomon (orange), the foldable clamp (blue) to set up the upper part at the right angle, depending on the latitude. Right: zoom-in showing the outlined rectangles of the surface mesh. (For interpretation of the references to colour in this figure legend, the reader is referred to the web version of this article.)

The pocket sundial was segmented in six ROI, corresponding to its main components: the lower housing with its pin that balances the compass needle, the upper folding ring with the corresponding hours, the hinge that connects the lower housing with the upper folding ring, the gnomon, the compass needle, and the foldable clamp that sets up the upper part at the optimal angle in dependence of the latitude (Fig. 4, left panel). The compass glass was excluded from the segmentation and later introduced as a virtual element (cf. below, Section 4.5.1). The wooden housing and the brass capsule of the chronometer were easily segmented due to their differing grey values, which were within clearly defined non-overlapping ranges. The interior of the chronometer, however, is characterised by a high degree of complexity and a fine structure. The majority of the small-scale mechanics are situated below the resolution of the employed CT instruments, making a precise segmentation hardly feasible. Additional approaches were therefore undertaken to render the internal mechanics of the chronometer (cf. Section 4.5.1). A total of 12 distinct ROI were defined for the barometer. The first eight include the upper and lower part of the leather case, the corresponding hinge that connects the aforementioned sections, the brass housing, the blue steel pointer, the aneroid cell, an installation panel with a mounting bracket. Further four ROI are attached to the mounting bracket: a metal plate that functions as a spring and changes its angle depending on the expansion of the aneroid cell, a lever that transmits the movement of the plate to a deflector pivot, which in turn pulls a chain on a spindle that is connected to the pointer.

4.4. Surface extraction

Once the required voxels have been assigned to their respective ROI, each element of the object can be represented by geometric surface models. The surfaces calculated from the ROI are typically represented by points arranged in triangulated meshes (Fig. 4, right). The Dragonfly software provides a straightforward method for calculating and extracting these surfaces. The surface mesh is generated using a Visualization Toolkit (VTK) / Object Research System (ORS) implementation of the Marching Cubes algorithm [33]. This algorithm traverses each voxel cube in the 3D dataset, compares the corner intensities against a user-defined isovalue, and linearly interpolates along intersected edges to construct a triangular surface mesh [34]. Common artefacts associated with this approach include stair-step or blocky surfaces due to voxel discretization, topological ambiguities, such as holes or spurious tunnels arising from certain cube configurations [35] and mesh quality issues like degenerate triangles, noise-induced roughness, and ex-

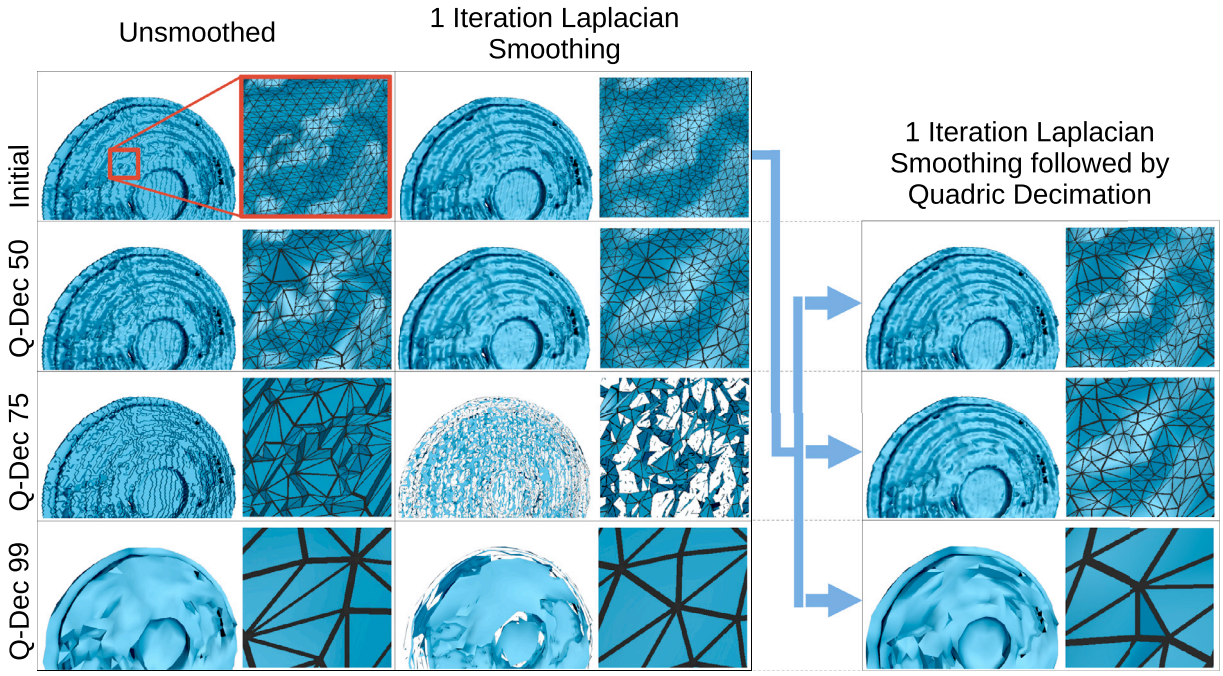

Fig. 5. Close-up of a part of the surface model of the aneroid cell of the pocket barometer derived from the CT scan at different manipulation states, rendered as solid surfaces. The zoomed-in images highlight the triangle arrangement. Left column: unsmoothed meshes after a Quadric Decimation of 0 % (initial), 50 %, 75 %, and 99 %. Centre column: same surfaces after one iteration of Laplacian Smoothing. Right column: Quadric Decimation of 50 %, 75 %, and 99 % applied after one iteration of Laplacian Smoothing.

cessive polygon counts. These factors may negatively impact downstream morphometric analyses and visualization fidelity [36] and are therefore addressed in more detail in Section 4.5.1.

In Dragonfly, the smoothness and density of the surface meshes are controlled by the 'threshold' and 'sampling' parameters in the 'Generate Contour Mesh' panel. The threshold parameter introduces a padding region to the ROI, with 100 corresponding to no padding and 0 to a maximum padding of 4 voxels in all directions from the ROI border. In this work, all surface meshes were generated with a threshold value of 50. The sampling parameter determines the rate at which the (padded) ROI voxels are sampled in the mesh. This defines the number of triangle vertices in the mesh, which has a huge implications for both the accuracy of the representation and the storage size of the model. Our surface models were generated sampling every two voxels in all directions.

4.5. Modification of surface meshes

In order to guarantee an uninterrupted and aesthetically pleasing experience of an object within a web application, modifications of the meshes are often required. The substantial storage requirements of high-resolution meshes derived from CT-measurement necessitate the simplification of intricate geometries, while ensuring the retention of the essential features of the object. As an example, we show how the number of triangles and the appearance of the barometer's aneroid cell surface model is affected by application of the 'Quadric Decimation' and 'Laplacian Smoothing' within the Dragonfly software (Fig. 5).

Quadric decimation reduces the surface mesh according to a parameter corresponding to the percentage reduction of the number of triangles. The algorithm computes a quadric error for each vertex, representing how far the vertex is from the original surface planes. It then selects edges to collapse based on the smallest increase in total error. This process reduces the polygon count while preserving the overall shape and features as much as possible [37]. We note, however, that the relationship between the number of triangles and the memory footprint is not linear and depends on the individual mesh geometry and connectivity, as shown in Section S1 of the Supplementary Information (SI). In our tests, reductions of up to 50 % were feasible without appreciable loss in surface quality. However, more aggressive reductions (e.g., 75 %, or 99 %) led to faulty meshes with defects such as holes or distortions (Fig. 5). This is primarily due to the discrete voxel size of the original CT data, which produces stepped surfaces vulnerable to damage when overly simplified.

To alleviate this problem, a 'Laplacian Smoothing' operation was applied to the mesh. This operation retains the initial number of triangles, while simultaneously modifying their dimensions and spatial arrangement. Our iterative testing showed that smoothing could be applied either before or after a 50 % decimation with no appreciable difference in surface appearance. However, application of larger reductions was only feasible after smoothing, since attempting to smooth overly reduced meshes inevitably leads to formation of voids and extended surface defects (Fig. 5). In the context of complex objects, such as chronometers with intricate inner components, it is imperative to employ a meticulous reduction approach, eschewing the utilisation of automated algorithms for the entirety of the model. Rather than directly in Dragonfly, the smoothing process was executed within the Blender software environment, utilising the sculpting tools to refine the surface and eliminate irregularities. Subsequently, decimation was performed to systematically reduce polygon density while preserving the object's shape. Finally, polygon modelling and additional smoothing were conducted in Blender's 'Edit Mode' or 'Sculpting Mode', enabling precise manual adjustments to specific areas requiring refinement. This iterative workflow –combining automated reduction with manual sculpting and refinement– was selected to optimally balance mesh complexity reduction and the preservation of critical surface details, ensuring that the final models are suitable for web visualisation without sacrificing accuracy. More information about the employed surface-modifying algorithms is reported in Section S2 of the SI.

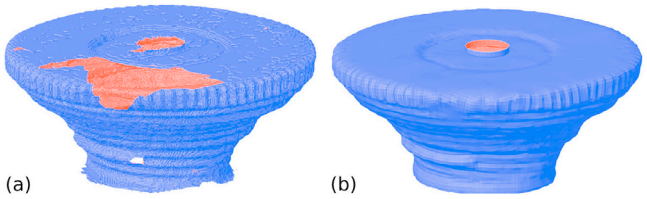

Fig. 6. Fusee surface model of the maritime chronometer: (a) original mesh showing a hole in its structure due to poor segmentation; (b) model after closing the hole, cleaning, smoothing, and reduction of triangles.

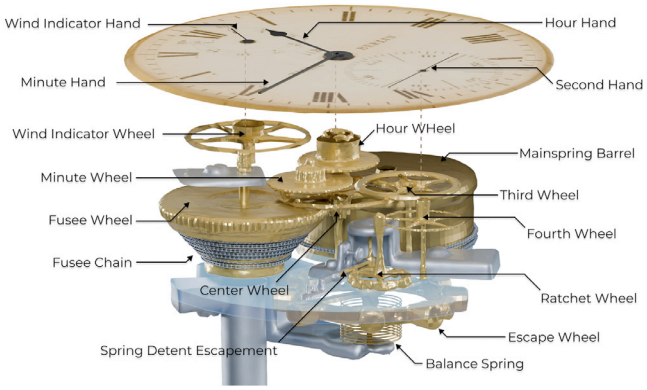

Fig. 7. Visualisation of the inner structure of the chronometer, annotated with descriptions of each individual component.

4.5.1. Repairing of surface mesh defects and simple geometric forms

Software solutions such as MeshLab, InstantMeshes, and Blender offer a variety of mesh editing options. Besides the ability to perform mesh reduction and refine the model's overall aesthetic by smoothing, as described above, they also permit the repair of intrinsic mesh errors and defects. Mesh errors that often occur during the data processing stages include non-manifold (non-watertight) geometries and overlapping vertices [38]. The latter can be effectively removed through the 'Merge by Distance' function in Blender. However, voids within the object can result from inadequate segmentation while still maintaining a so-called watertight mesh. As illustrated in Fig. 6a, the fusee surface of the maritime chronometer was poorly segmented and presented an extended hole defect. This hole could be closed using the 'Screened Poisson Surface Reconstruction' algorithm of MeshLab, based on [39]. Furthermore, the '3D Print Toolbox' add-on in Blender, and in particular the 'Sculpting' and 'Polygonal Modelling' toolsets, are very useful for identifying and resolving mesh defects. Application of such tools results in much improved appearance of the models' surfaces (i.e., Fig. 6 b).

To save memory, some surface parts can be replaced with simple geometric shapes. For example, the base plate inside the maritime chronometer does not require a high resolution and was therefore replaced with a flat cylinder. This is also essential to represent very fine structural features below the CT resolution limit, as it was the case for the chronometer's balance spring, which was replaced by a thin, spiralled cylinder (cf. Fig. 7). Also the thin clock hands could not be properly resolved in the original CT scan, and had to be remodelled in Blender. To do so, a 2D image of the clock face was loaded into Blender as a plane, then each hand was given an off-plane thickness to create 3D objects. The hands were then removed from the image using the GIMP image editing software to preserve the bare background (Fig. 7). This technique was also employed for the Roman numerals of the pocket sundial, which replaced the almost undiscernible engraving on the surface model (cf. the photograph in Fig. 2a, the surface model based on the CT scan in Fig. 4 and the final result in Fig. 9). While the use of Blender was very practical in our workflow, we note that 3D parts can be repaired or constructed using any CAD software of choice, provided that the necessary licences are available and the file formats are compatible.

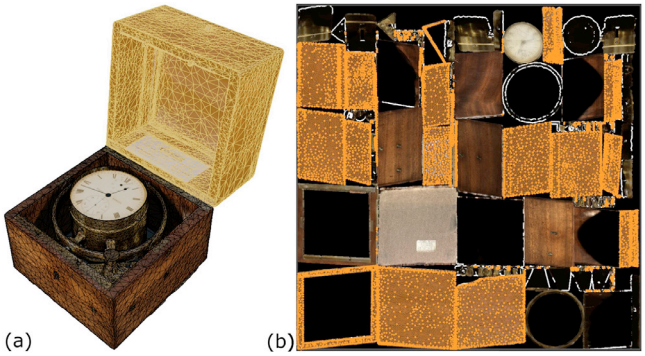

Fig. 8. Maritime chronometer: (a) triangulated surface mesh based on structured-light measurements and X-ray CT; (b) corresponding *UV* map with a transferred 4K texture map. Highlighted parts represent vertices on the mesh surface along with their corresponding *U* and *V* coordinates.

4.5.2. Texturing and structured-light 3D measurements

The surface models obtained via X-ray CT measurements do not contain information about the original material texture, which thus needs to be applied afterwards to the digital representation. In this process, one can either aim to obtain a photorealistic look of the model or deliberately choose non-natural textures and colours to highlight particular components of the object (as done i.e. in Fig. 4 to distinguish between the different parts of the pocket sundial).

The advantage of bestowing the CT scan with a virtually infinite palette of digital materialities cannot be overestimated. The use of different colour codes for static and non-static parts (Fig. 7), or of semi-transparent renderings to allow a view into the interior of the objects, has a great pedagogical value, besides its mere aesthetic appeal (i.e. the final results of our web implementations in Fig. 9a). Various realistic material textures can be created in Blender, including highly reflective materials, such as metals and glass. For instance, a realistic-looking glass material can be obtained via the Principled BSDF shader with the following parametric values: Metallic 0.975, Roughness 0.05, IOR 2.0, Alpha 0.26.

In order to authentically reproduce non-homogeneous textures and colour shading of an object's exterior (such as the precise veins of the wooden case of the maritime chronometer), CT scans can be enriched with high-resolution texture maps acquired with structured-light 3D scanner measurements. These are particularly advantageous for surfaces exhibiting low reflectivity and complex textures. As for the surface meshes, also in this case it is necessary to strike a balance between mesh and texture resolution on one side and file size on the other side for the subsequent use of the models in web and mobile platforms. For example, the initial high-resolution model of the maritime chronometer generated using structured-light 3D scanner measurements contained approximately 16 million polygons, 73 texture files and a file size of 1.89 GB. Web and mobile platforms, however, typically require file sizes under 10 MB and polygon counts of the order of 100,000. To match those requirements, we exploited Blender's *UV* mapping and texture baking capabilities. The *UV* map (Fig. 8b) is a 2D representation of the 3D object's surface, obtained by unwrapping the mesh surface into planar coordinates. Texture baking enables the transfer of details such as lighting, shading, and surface textures from a high-resolution 3D model to a low-resolution version by precomputing and embedding this information into texture maps with reduced resolution (in our case, 4096×4096 pixels). Moreover,

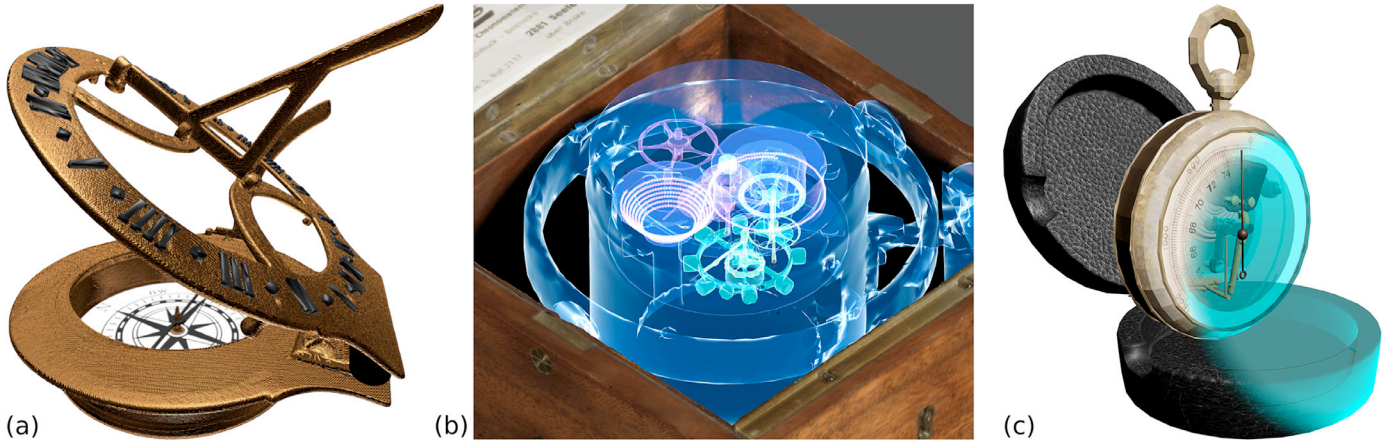

Fig. 9. Screenshot images of the web applications of the historical measuring instruments: (a) pocket sundial after animation of the unfolding process; (b) Tiede's maritime chronometer after animation of the opening, disassembling, and activating of a translucent view; (c) Lufft pocket barometer after opening the case and lifting up with the X-ray-view turned on to see the interior.

Blender allows for filling in or cleaning up flawed texture information. The final optimised model achieved a file size of 7 MB and a polygon count of 180,000, achieving a good balance between retention of visual details and computing performance.

The so-obtained surface map can be superimposed onto the CT surface model using Blender, enabling a seamless integration of structured-light scanning and X-ray CT into photorealistic digital object representations (Fig. 8a).

4.6. Implementation of web applications

The digital objects obtained through CT measurements and enriched with structured-light scanning information form the basis for interactive web applications, in which users can observe, manipulate, and learn about the objects on computer screens and in virtual reality environments. To this aim, first the objects are prepared for interactive or predefined animations, and then web environments are set up as user/object interfaces.

4.6.1. Adding animations to the rendered objects

Animations can be realised in multiple ways in Blender. Common is the 'keyframe' method, which requires the definition of starting and end positions of the object elements achieved by adjusting the element location values in the 'Transform' panel of Blender. Afterwards, the desired number of intermediate key frames defining the element motion is generated by the software [40].

In order to illustrate the rotational movements of the chronometer's gears, it was necessary to establish the pivot points for each movable component. These pivot points must be positioned with precise accuracy at the element's centre of mass in order to facilitate smooth and accurate rotation. Notwithstanding the fact that Blender's 'Set Origin to Centre of Mass' function provides a starting point, it frequently necessitates manual adjustment to achieve the required precision. Afterwards, the relative rotational speed of each wheel in the chronometer's clockwork was calculated, taking into account that the distance moved by their teeth is proportional to their diameters, and that the tangential speed of connected wheels must be the same. This imposes a mutual constraint to their relative motion expressed by $T/d = constant$, with T the rotational period and d the diameter of each connected gear. It should be noted that these calculations are approximate due to the limited resolution of the CT data; however, they are sufficiently accurate to create a coherent animation for web display.

The slow motion of certain components with respect to others, for instance the rotation of the wheel associated with the hour hand of the chronometer, results in a very large number of key frames and thus in excessively large data set sizes. For this reason, the animation of each part (e.g. of each chronometer gear wheel) was exported as a short clip, while the playback speed was dynamically controlled via JavaScript in the web application. Compression of the animated files up to 90 % was realised using the Draco compression library (GLB format).

4.6.2. Web-based interaction with the digital objects

The web interactions with the objects were implemented with three.js, ensuring the compatibility of the applications with common mobile and desktop browsers. The source code for the three representations is hosted in repositories on GitHub and GitLab [41–43]. Each application consists of a main scene, light sources, and a virtual camera through which the object is viewed. The 3D models were optimised for viewing on mobile devices by decimating the geometry and saving the resulting files in the binary GLTF format, which can be easily loaded by three.js. All scenes feature both mouse and touch controls for viewing the objects from all angles and controlling the animations. More detailed information about basic scene setting in three.js is provided in the SI, Section S2.

The digital representation of the pocket sundial includes a brass-like surface rendering of the folded device, which can be zoomed in and out, rotated in all directions, and unfolds upon clicking a dedicated button activating an animation of the gnomon and bracket (Fig. 9a) [44]. Another button activates an animation in which a rotating light source casts a gnomon shadow on the hour ring, thus simulating the function of the sundial with passing time. The SI, Section S2, reports more information about the shadow projection.

The chronometer is part of a larger application with different modes of interaction, which is now integrated in the digital collection and exhibition of the German Maritime Museum in Bremerhaven [45]. A first interaction mode is a text-based quiz feature used to learn about the names, function, and relevance of multiple elements of the chronometer [46], as researched by the curators of the German Maritime Museum. The basis for the quiz questions is a set of clickable annotations placed around the object, ordered in different thematic categories, such as globalisation, the connection between humanity and the sea, the technological aspects, and the object's history. A second mode is an augmented-reality environment where users can use the camera of their mobile devices to virtually place the model on top of a table in front of them

and closely inspect its numerous individual components. Appealing visualisations of the chronometer's interior (Fig. 9b) highlight the particularly fine quality of the clockwork and the intricacy of the mechanical gears, which have been carefully reconstructed in the digital representation (Fig. 7). The web application enables digital disassembly of the gear box and observation of the operational functionality of the chronometer, revealing the movement of the cogwheels and the rotation of the hour and minute wheels. The harmonious integration of photorealistic representations of the external wooden case, the clock face and the digitally assigned material surfaces of the internal components produces an aesthetically pleasing outcome.

Finally, the barometer is represented in an application that illustrates its functionality [47]. The case can be opened and hidden, and the barometer lifted up in order to gain a better view of the object of interest. The 'X-Ray' option provides users with the ability to discern the internal mechanisms by following the movement of the mouse cursor over the object (Fig. 9c). Activation of the measuring mechanism is initiated by pressing the button, thereby simulating a change in air pressure. This results in the barometer's membrane undergoing expansion or contraction, consequently actuating the pointer on the upper side via a deflection mechanism. The illustration of the original dial, when viewed in conjunction with the simplified geometry and the artificially created surface, provides a comprehensive understanding of the object's design and functionality. The option of displaying the case contributes to the authentic presentation of the barometer and conveys an informative impression about the different materialities of the case and the instrument.

5. Discussion

5.1. Historical objects and their digital representations

By the 16th and 17th centuries, pocket sundials had become a popular accessory among the educated elite in Europe. These devices remained in use until the widespread adoption of mechanical clocks in the 17th and 18th centuries. They were regarded as both practical and symbolic items, reflecting the cultivated lifestyle and scientific affinity of those who owned them. Our digital representation of the sundial places emphasis on its shiny brass material and its simple, elegant design. We have avoided the inclusion of too many intricate details below the CT resolution limit and reconstructed some of the elements, such as the Roman numerals. While the decision to present the latter in relief rather than engraved is to some extent arbitrary, the model could be used to reproduce the instrument with 3D printing and enable its manipulation by visually impaired people. The fabrication of sophisticated 3D models is conceivable, in which microcontrollers could track its movements and provide real-time feedback to the observers. A further improvement of our digital representation, beside the already implemented function under sunlight, would be the consideration of the sun's altitude dependent on latitude and time. Additionally, the behaviour of the magnetic needle with respect to the sun's orientation could be reproduced.

Christian Friedrich Tiede's maritime chronometers hold profound significance in the history of maritime navigation. These precision instruments played a pivotal role in the evolution of navigation during the 19th century, facilitating the accurate determination of longitude at sea. Tiede's chronometers were constructed with meticulous attention to detail and utilised the finest materials of the time. They were renowned for their reliability and precision, with mechanisms designed to withstand the rigours of maritime travel. They facilitated scientific exploration, trade expansion, and cultural exchange, playing pivotal roles in historical expeditions, and shaping global commerce. As artefacts of technological innovation and maritime heritage, Tiede's chronometers exemplify not only the scientific and cultural significance of their era but also the materiality of craftsmanship and innovation that defined 19th-century horology. The very fine and precise construction represents a challenge for CT measurements and the subsequent segmentation. The instrument's size and metallic composition necessitated high X-ray energy, at the expense of spatial resolution. For this reason, some of the gear's components were artificially recreated. The materiality and appeal of the wooden box's surface have been faithfully preserved by combining structured-light scanning techniques with CT. In this way, the outer appearance is identical to the original object, but its interior becomes accessible, allowing for a wholly novel degree of engagement with the fine mechanics and principle of operation of the instrument.

The third instrument of our study, the pocket barometer, was able to detect changes in atmospheric pressure due to deformations of the aneroid cell, which translate into alterations of the tension experienced by the pointer. The presence of the word 'COMPENS.' on the dial indicates that the altimeter incorporates a mechanism of compensation for temperature variations, thereby ensuring the accuracy of the readings in a wide temperature range. This mechanism involved the use of strips composed of two metals with distinct coefficients of thermal expansion joined together (typically, beryllium-copper alloys) forming the aneroid cell. Unfortunately, the employed CT instruments did not resolve the slight differences in X-ray absorption within the bimetallic strips. However, the primary functionality of the digital object could be well represented, as is the contrast of materialities of the instrument and its enclosing leather case. If wished, post-processing techniques, such as colour enhancement, could be employed to highlight the hidden materialities. Moreover, the digital representation could virtually reproduce the measurement of altitude based on imposed changes of air pressure in the web application.

5.2. Technical workflow

The final result of the digital representation obviously depends on the details of the entire technical workflow of CT and structured-light measurements, reconstruction, segmentation, surface extraction, modification and repair, before implementation into the web application. Limits to the resolution of the images depend both on the availability of appropriate instrumentation and on the combination of materials (e.g. metals vs wood or paper) and part sizes (e.g. fine vs coarse and large parts) in the object. The application of one or a sequence of different filter processes to the images subsequent to the measurement and reconstruction can serve to enhance the quality of the CT images, reduce or eliminate possible artefacts (cf. Fig. 3), and facilitate the subsequent process of segmentation. In this process, the filter type and sequence should be able to both preserve sharp object edges and maintain a smooth appearance of homogeneous areas. The entire process can be very time consuming. The X-ray measurements take up from a few hours to a day per object and often need to be repeated with different parameters to achieve the desired quality. The segmentation process, especially if performed manually, the surface modifications and the final rendering in web applications can take up to several days per object, depending on object complexity, target rendering quality, and user experience with the various software tools.

The process of segmentation is the most pivotal and often the most time-consuming step in the data analysis workflow. The complexity and quality of the individual data set play a significant role in determining the required time and resources. In the case of objects comprising clearly distinct grey value ranges across their constituent parts, an expedited segmentation process can be accomplished by means of a thresholding approach. In the case of

overlapping grey value ranges, however, manual segmentation on a slide-by-slide basis is still the method of choice. The implementation of deep-learning tools in segmentation software (including Dragonfly) is promising, especially for the identification of recurring patterns within the TIFF stack. However, during the segmentation of individual fine mechanical components of our technical historical objects, such tools have been found to be of rather limited utility.

No matter the quality of the segmentation, a subsequent step of surface modification is unavoidable, in particular to simplify the meshes and reduce the size of the data sets. Many algorithms are available for this purpose, among which are the pioneering algorithms by Garland [37] for mesh reduction, or the volume-preserving Laplacian Smoothing by Taubin [48]. The necessity and type of mesh optimisation are dependent upon several factors, including the voxel size used in the CT measurements, the fineness of the structures of the object, and the memory size limits for the later applications. In many instances, it may be appropriate to perform Laplacian Smoothing prior to the Quadric Decimation, rather than the reverse, as seen in Fig. 5. This results in more appealing models with reduced step-like artefacts and smaller data sizes. Alternatively, to reduce such artefacts –particularly for very fine structures such as the interior of the barometer– upsampling of the grey value data set can be performed prior to segmentation. Provided the availability of sufficient memory, upsampling results in the reduction of voxel sizes, enhancing the simulated resolution and improving the final outcome after mesh reduction and smoothing.

To ensure robust and visually accurate rendering in interactive and real-time applications, it is essential that 3D surface meshes are topologically watertight – meaning that they form a closed, manifold surface without gaps, holes, or spurious edges. Watertight meshes enable rendering engines to unambiguously define inside and outside regions of an object, which is critical for the correct computation of surface normals and lighting interactions. Physically-based rendering techniques, such as ray tracing, global illumination, and subsurface scattering, rely on this topological integrity to simulate realistic light behaviour. In contrast, non-watertight models may lead to rendering artefacts, including incorrect shading, lighting leaks, and unexpected transparencies. Furthermore, watertightness improves compatibility with compression algorithms such as Draco, facilitates efficient GPU memory usage, and prevents visual errors during animation or user interaction. Thus, ensuring watertight geometry is a fundamental prerequisite for the reliable visualisation and deployment of 3D models in web-based and immersive environments.

While mesh reduction and surface manipulation are necessary for optimising the models for real-time rendering and web deployment, we are aware that these operations can alter the geometry of the original data. Our aim was to strike a balance between preserving the scientific integrity of the CT-derived geometry and achieving a visually coherent and accessible digital representation. To this end, any manual reconstructions or smoothing steps were limited to areas where the resolution of the original data already introduced uncertainty (e.g., surface noise, stepped edges, or artefacts from segmentation). Regions with fine structural detail or scientific relevance were handled with extra care, applying only local adjustments when needed. The final models thus preserve the essential geometric characteristics of the objects while providing an aesthetically pleasing and technically efficient representation suitable for public communication.

The final online presentation of the objects offers unlimited possibilities to creative curators of online applications and exhibitions. The interaction of the observer with the digital representations modifies their perception, making them an active protagonist in the knowledge acquisition process. The materiality and appearance of the objects can be digitally modified in order to enhance their visual appeal or to highlight important technical details. Digital inspection of fragile or packaged historical objects becomes possible, fostering a more intimate relationship between the object and the observer. The functionality of measurement instruments can be faithfully reproduced and more comprehensively grasped, even when the physical objects are not operational due to damaged components or missing parts.

The remote accessibility of the online applications opens them to individuals of all regions, ages and abilities. We hope that this work will encourage those engaged in research involving 3D museum data to present their findings in appealing and user-friendly formats. However, it is important to note that the creation of interactive web applications and their integration into digital museum collections requires both substantial human labour and the availability of sufficient technical hardware capacity. Additionally, it is essential to consider long-term archiving strategies for the digital object, comparable to those employed for the original objects.

6. Conclusions

The present study has detailed a comprehensive and user-friendly workflow for the use of data obtained from computed tomography and structured-light scanning for purposes beyond scientific research. The digitalisation of technical objects of cultural heritage interest opens up new interaction channels with interested observers, enabling virtual manipulation, the acquisition of new knowledge, and the appreciation of technical details of historical value. This is especially valuable for research museums, which can include the digital object representation in standalone online exhibitions or use them in media stations situated in close proximity to the original object, enhancing the museum's experience. Being able to observe or even operate ancient maritime instruments from anywhere in the world bestows them with novel virtual life and lets them continue their navigation in both space and time.

Acknowledgements

This research was conducted as part of the DigitalMaterialities project funded by the Leibniz Association under project number T91/2020. The investigated objects are part of the collection of the German Maritime Museum – Leibniz Institute for Maritime History. CT measurements were performed with the instruments of the MAPEX Center for Materials and Processes and the Fraunhofer Institute for Integrated Circuits IIC. The authors would like to express their gratitude to Frederic Theis for his profound insights into the chronometer's operational mechanics. Additionally, we would like to acknowledge Amr Okdeh and Mahmmoed Al Kotob for their contributions to the animation of the chronometer as part of their bachelor's thesis.

Supplementary material

Supplementary material associated with this article can be found, in the online version, at 10.1016/j.culher.2025.09.007

References

[1] C. Wilson-Barnao, Digital Access and Museums as Platforms, Routledge, 2022. First edition
[2] K.E. Rankin, Z.J. Hazell, A.M. Middleton, M.N. Mavrogordato, Micro-focus X-ray CT scanning of two rare wooden objects from the wreck of the London, and its application in heritage science and conservation, J. Archaeolog. Sci. Rep. 39 (2021) 4054–4069.
[3] R. Furferi, L.D. Angelo, M. Bertini, P. Mazzanti, K. De Vecchis, M. Bif, Enhancing traditional museum fruition, current state emerg. tend., Heri. Sci 12 (2024) 20.

[4] E. Champion, H. Rahaman, Survey of 3D digital heritage repositories and platforms, Virtual Archaeol. Rev. 11 (23) (2020) 1–15.
[5] E. Champion, H. Rahaman, 3D digital heritage models as sustainable scholarly resources, Sustainability 11 (8) (2019) 2425.
[6] K. Niven, J.D. Richards, The Storage and Long-Term Preservation of 3D Data, Elsevier Inc., 2017.
[7] C. Portalés, J. Lerma, C. Pérez, Photogrammetry and augmented reality for cultural heritage applications, Photogramm. Rec. 24 (128) (2009) 316–331.
[8] H. Rahaman, E. Champion, To 3D or not 3D: choosing a photogrammetry workflow for cultural heritage groups, Heritage 2 (3) (2019) 1835–1851.
[9] Sketchfab, The leading platform for 3D and ar on the web, 2024, https://www.sketchfab.com/, Last accessed on 2025-03-05
[10] G. Wang, H. Yu, B. De Man, An outlook on X-ray CT research and development, Med. Phys. 35 (3) (2008) 1051–1064.
[11] N. Aslan, B. Ceylan, M.M. Koç, F. Findik, Metallic nanoparticles as X-ray computed tomography (CT) contrast agents: a review, J Mol Struct 1219 (2020) 128599.
[12] K. Aragishi, Y. Takeda, Y. Suzuki, A. Matsumoto, Study on the deformation and fracture of epoxy monoliths through mechanical tensile and compressive tests and X-ray CT imaging, Polym. J. 56 (5) (2024) 529–540.
[13] P.J. Withers, C. Bouman, S. Carmignato, V. Cnudde, D. Grimaldi, C.K. Hagen, E. Maire, M. Manley, A.D. Plessis, S.R. Stock, X-ray computed tomography, Nat. Rev. Methods Primers 1 (1) (2021) 18.
[14] T. De Mil, J.V.d. Bulcke, Tree core analysis with X-ray computed tomography, J. Visualized Exp. 199 (2023) e65208.
[15] R.M. Lieb-Lappen, E.J. Golden, R.W. Obbard, Metrics for interpreting the microstructure of sea ice using x-ray micro-computed tomography, Cold Reg. Sci. Technol. 138 (2017) 24–35.
[16] M.J. Munawar, C. Lina, V. Cnuddec, T. Bultreys, C. Dong, X. Zhang, W. De Boever, M.A. Zahid, Y. Wu, Petrographic characterization to build an accurate rock model using microct: case study on low-permeable to tight turbidite sandstone from Eocene Shahejie Formation, Micron 109 (2018) 22–33.
[17] J. Dinley, L. Hawkins, G. Paterson, A.D. Ball, I. Sinclair, P. Sinnett-Jones, S. Lanham, Micro-computed X-ray tomography: a new non-destructive method of assessing sectional, fly-through and 3D imaging of a soft-bodied marine worm, J. Microsc. 238 (2010) 123–133.
[18] A. Krüger, S. Slater, V. Vajda, 3D imaging of shark egg cases (Palaeoxyris) from sweden with new insights into early Jurassic Shark Ecology, GFF 143 (2021) 229–247.
[19] K. Duncan, K. Czymmek, N. Jiang, A. Thies, C. Topp, X-ray microscopy enables multiscale high-resolution 3D imaging of plant cells, tissues, and organs, Plant Physiol. 188 (2) (2022) 831–845.
[20] Z. Zhang, Z. Zhang, J. Ma, P. Taylor, L. Strotz, S. Jacquet, C. Skovsted, F. Chen, J. Han, G. Brock, Fossil evidence unveils an early cambrian origin for Bryozoa, Nature 599 (7884) (2021) 251–255.
[21] J.M. Warnett, M.A. Williams, P.F. Wilson, M.P. Smith, The oxford dodo. seeing more than ever before: X-ray micro-CT scanning, specimen acquisition and provenance, Hist. Biol. 39 (2020) 2247–2255.
[22] A. Fostriropoulou, A. Karatzani, Study of a pair of traditional women's shoes from Chios Island dated to 1905, Archaeology (1) (2021) 14–20.
[23] F. Albertin, L. Baumer, M. Bettuzzi, R. Brancaccio, E. Caruso, F. Casali, L. Cifarelli, G. Festa, M. Griffo, A. Mistretta, M. Morigi, R. Nania, A. Parrinello, L. Strolin, X-ray computed tomography to study archaeological clay and wood artefacts at Lilybaeum, Eur. Phys. J. Plus 136 (3) (2021) 1–29.
[24] R. Abel, C. Laurini, M. Richter, A palaeobiologist's guide to 'virtual' micro-CT preparation, Palaeontol. Electronica 15 (2) (2012) 6T.
[25] J.W. Adams, A. Olah, M. McCurry, S. Potze, Surface model and tomographic archive of fossil primate and other mammal holotype and paratype specimens of the ditsong national museum of natural history, Pretoria, South Africa, PLoS ONE 10 (10) (2015) e0139800.
[26] M. Tesařová, E. Heude, G. Comai, T. Zikmund, M. Kaucká, I. Adameyko, S. Tajbakhsh, J. Kaiser, An interactive and intuitive visualisation method for X-ray computed tomography data of biological samples in 3D portable document format, Sci. Rep. 9 (2019) 14896.
[27] X-AID, Software for scientific and industrial CT, 2024, (https://www.x-aid.de/, Last accessed on 2025-03-05.
[28] Dragonfly, Turning images into insights.(2022). https://www.dragonfly.comet.tech/, Last accessed on 2025-03-05.
[29] Blender, Blender about, 2024, https://www.blender.org/about/, Last accessed on 2025-03-05.
[30] threejs, Javascript 3D library, 2024, https://www.threejs.org/manual/#en/fundamentals, Last accessed on 2025-03-05.
[31] Y. Liu, R. Xie, L. Wang, H. Liu, C. Liu, Y. Zhao, S. Bai, W. Liu, Fully automatic ai segmentation of oral surgery-related tissues based on cone beam computed tomography images, Int. J. Oral Sci. 16 (2024) 1–12.
[32] E.T.V. Bezerra, K.S. Augusto, S. Paciornik, Discrimination of pores and cracks in iron ore pellets using deep learning neural networks, Revista Escola de Minas 73 (2020) 197–203.
[33] ORS team, OrsMarchingCube — Generates mesh from ROIs using the VTK/ORS marching cubes algorithm (2020). https://dev.theobjects.com/dragonfly_2020_2_release/OrsPythonPlugins/OrsMarchingCube/sphinxIndexOrsMarchingCube.html, Dragonfly v2020.2 documentation, last accessed on 2025-07-17.
[34] W.E. Lorensen, H.E. Cline, Marching cubes: a high resolution 3d surface construction algorithm, SIGGRAPH Comput. Graph. 21 (4) (1987) 163–169.
[35] G.M. Nielson, B. Hamann, The asymptotic decider: resolving the ambiguity in marching cubes, in: Proceedings of Visualization '91, 1991, pp. 83–91.
[36] T.S. Newman, H. Yi, A survey of the marching cubes algorithm, Comput. Graph. 30 (6) (2006) 854–879.
[37] M. Garland, P.S. Heckbert, in: Surface simplification using quadric error metrics, 1997. In G. Scott Owen, Turner Whitted, and Barbara Mones-Hattal, editors, Proceedings of the 24th Annual Conference on Computer Graphics and Interactive Techniques, SIGGRAPH 1997, Los Angeles, CA, USA, August 3-8, 1997, pages 209–216. ACM
[38] G.E. Farin, Curves and Surfaces for Computer-aided Geometric Design - a Practical Guide, Series in Computer Graphics, 5th ed., Morgan Kaufmann, 2001.
[39] M. Kazhdan, H. Hoppe, Screened poisson surface reconstruction, ACM Trans. Graph. 32 (29) (2013) 1–29. 13
[40] R. Parent, Computer Animation - Algorithms and Techniques, 3rd ed., Morgan Kaufmann, 2012.
[41] Repository pocket sundial, 2024a, https://www.gitlab.com/melameddavid19/threejs_portable_sundial, Last accessed on 2025-03-05.
[42] Repository maritime chronometer, 2024b, https://www.github.com/dsm-museum/artefact, Last accessed on 2025-03-05.
[43] Repository pocket barometer, 2024c, https://www.github.com/k00lthing/seamans-gear-hackaton, Last accessed on 2025-03-05.
[44] Sundial, Interactive web application of a pocket sundial(2023). https://www.threejs-portable-sundial.vercel.app/, Last accessed on 2025-03-05.
[45] Chronometer, Interactive web application of a maritime chronometer (2024). https://www.3d.dsm.museum/ar_dev#/models/chronometer, Last accessed on 2025-03-05.
[46] I. Hodgson, D. Hoffmann, L. Junge, F. Theis, N. Dittgen, Learning to listen properly: participatory digital projects at the german maritime museum based on iterative co-creation, J. Comput. Cult. Herit. 17 (3) (2024) 51.
[47] Barometer, Interactive web application of a pocket barometer.(2022). https://www.seamans-gear-hackaton.vercel.app/, Last accessed on 2025-03-05.
[48] G. Taubin, Curve and surface smoothing without shrinkage, in: Proceedings of the Fifth International Conference on Computer Vision (ICCV 95), Massachusetts Institute of Technology, Cambridge, Massachusetts, USA, June 20–23, 1995, pages 852–857. IEEE Computer Society, 1995.